Light-Induced Increase of Electron Diffusion Length in a p-n Junction Type $CH_3NH_3PbBr_3$ Perovskite Solar Cell

Nir Kedem[1,*], Thomas M. Brenner[1,*], Michael Kulbak[1], Norbert Schaefer[2], Sergiu Levcenko[2], Igal Levine[1], Daniel Abou-Ras[2], Gary Hodes[1], David Cahen[1]

*equal contribution

1. Dept. of Materials & Interfaces, Weizmann Inst. of Science, Rehovot, Israel 76100

2. Helmholtz-Zentrum Berlin für Materialien und Energie GmbH, Hahn-Meitner-Platz 1, 14109 Berlin, Germany

ABSTRACT:

High band-gap, high open-circuit voltage solar cells with methylammonium lead tri-bromide ($MAPbBr_3$) perovskite absorbers are of interest for spectral splitting and photo-electrochemical applications, because of their good performance and ease of processing. The physical origin of high performance in these and similar perovskite - based devices remains only partially understood. Using cross-section electron-beam-induced current (EBIC) measurements, we find an increase in carrier diffusion length in $MAPbBr_3$(Cl)-based solar cells upon low intensity (~few % of 1 sun intensity) blue laser illumination. Comparing dark and illuminated conditions, the minority carrier (electron) diffusion length increases about 3.5 times from L_n = 100 ± 50 nm to 360 ± 22 nm. The EBIC cross-section profile indicates a *p*-*n* structure between the *n*-FTO/TiO_2 and *p*-perovskite, rather than the *p*-*i*-*n* structure, reported for the iodide derivative. Based on the variation in space-charge region width with varying bias, measured by EBIC and capacitance-voltage measurements, we estimate the net-doping concentration in $MAPbBr_3$(Cl) to be 3-6x10^{17} cm^{-3}.

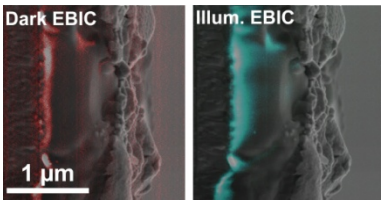

MAIN TEXT:

Methyl ammonium lead tri-bromide ($MAPbBr_3$) based perovskite solar cells have attracted less attention than the iodide derivative. The relatively high band gap of 2.3 eV limit the maximum theoretical efficiency to ~16% within the Shockley-Queisser model. However, with demonstrated open-circuit voltages (V_{oc}) as high as 1.4-1.5 V[1–4], these solar cells show great potential for use in tandem or spectral splitting applications[5,6] as well as for electro-chemical water splitting.[7–9] The demonstrated power conversion efficiencies reach values of 9%, with V_{oc} as high as 1.5 V and short-circuit current density, j_{sc}, as high as 9 mA/cm^2 (approaching the theoretical maximum).[1,2]

Similar to the structure of $MAPbI_3$ solar cells Br-perovskite layers are stacked between a hole blocking layer, commonly TiO_2, and a hole-transport layer (HTL). For $MAPbI_3$ 2,2'7,7'-tetrakis-(N,N-di-p-methoxyphenyl amine)-9,9'–spirobifluorene is commonly used as HTL, whereas in this work 4,4'-bis(N-carbazolyl)-1 ,1' –bisphenyl (CBP) was used for high V_{OC} $MAPbBr_3$ cells. In the past, this type of stacking has been shown to exhibit *p-i-n* device characteristics for the $MAPbI_3$-based cells, using electron-beam-induced current (EBIC)[10,11] measurements as well as impedance spectroscopy and time-resolved pump-probe techniques.[12–14] In this case, EBIC analysis provided some of the first experimental evidence for the *p-i-n* mechanism as well as for the unusually long and balanced carrier drift/diffusion lengths, L_n and $L_{p,}$ for electrons and holes, respectively. Whether the working mechanism for $MAPbBr_3$-based photovoltaic devices is the same as that of their iodide analogs has not yet been established.

EBIC measurements have been demonstrated in the past to be an effective tool to resolve the built-in fields and carrier diffusion lengths in semiconductor junctions[15]. In this method, a focused electron beam scans across the junction area generating excitons, which upon splitting into free carriers, are collected through contacts to the sample. The low exciton binding energy of the perovskite ensures that nearly all the excitons dissociate at room temperature.[16–18] A current collection efficiency image can be formed by synchronizing the beam position with the collected current. The current vs. position profile obtained across the junction can indicate the location of built-in fields

and be used to determine carrier drift/diffusion lengths (depending on if a built-in field exists in the material or not). Signal decay rate with distance in the sample in the most general way can be regarded as 'collection length' and its interpretation depends on the working mechanism of the device, as will be discussed below and in the SI (S.1).

Some basic properties of $MAPbI_3$ and $MAPbI_3(Cl)$[19] reported in the literature have been shown to change dramatically upon illumination. There are several reports of long drift/diffusion lengths[20,21], with one report showing data that are interpreted as a decreased drift/diffusion length with increased light intensities[22]. The decrease is explained by an increased recombination rate when the photoexcited carrier concentration is too high. In another work the photoconductivity of $MAPbI_3$ is shown to change with time; alignment of the MA molecule followed by a slow relaxation of the inorganic cage is suggested as an explanation[23]. The dielectric constant of the material has also been reported to change upon illumination and to increase monotonically with light intensity up to one sun[24]. These changes upon illumination suggest that the "dark" material and the illuminated perovskite do not present similar working regimes. Several theoretical works[25–27] suggest a photoferroic effect, in which polarized domains efficiently separate charge at the nanoscale. These domains are assigned either to collective alignment of the organic cation or to the position of the metal ion. Hysteretic non-linear dark *I-V* curves in $MAPbI_3$ were interpreted as evidence for ferroelectricity.[28] However, experimental evidence specifically for a photoferroic effect has not appeared. An additional mechanism that may explain an increase in collection efficiency is suggested by observation of a switchable photovoltaic effect in a symmetric Au-perovskite-Au device configuration[29]. The charge separation mechanism was assigned to formation of a *p-i-n* junction due to ion drift, similar to what is the case in a light-emitting electrochemical cell and in general in mixed ionic-electronic conductors[30,31]. Although most work focused on $MAPbI_3$ or a mixed halide perovskite containing Br or Cl, as $MAPbBr_3$ is isostructural with $MAPbI_3$ we can reasonably assume that $MAPbBr_3$ will exhibit similar behavior, and the same can be said of $MAPbBr_3(Cl)$. Although quite common in organic molecules and semiconducting polymers[32,33], profound changes in material structure and transport properties

are not usually considered for inorganic semiconductors. More specific to EBIC analysis, this raises the question of how, if at all, the response of the material will change upon background illumination.

Previous reports[10,34,35] used EBIC as a tool to unravel the working mechanisms of photovoltaic devices. These measurements are normally done such that the only source of excitation is the electron beam. This has previously been considered to represent the solar cell function under short-circuit conditions. In view of the growing evidence (above) that perovskite material properties are dependent upon illumination, EBIC analysis should ideally be performed under solar cell standard operating conditions. As a first step towards this, in the present work solar cells with a planar, fluorine-doped tin oxide (FTO)/ dense-TiO_2/ $MAPbBr_3(Cl)$/ CBP/ Au stacking sequence were studied by means of EBIC under illumination and applied bias, as well as by capacitance-voltage measurements. We find that the EBIC profiles extracted across cross-sections of $MAPbBr_3(Cl)$ solar cells demonstrate that these cells exhibit characteristics of a *p-n* junction, rather than that of a *p-i-n* junction, as reported for $MAPbI_3$ and $MAPbI_3(Cl)$. This finding is confirmed by capacitance-voltage profiling. Application of supra-band gap background illumination during EBIC measurements shows a similar behavior, but with significantly increased minority-carrier diffusion lengths.

In order to perform EBIC under illumination and bias, the solar cells were first cleaved to expose the device cross-section. A special specimen holder was constructed in order to allow for simultaneous irradiation of the cell cross section with the electron beam and illumination with the light source. Figure 1 shows the layer stack of the $MAPbBr_3(Cl)$ solar cells, together with the position of the electron beam and of the light source. An optical fiber was used to transfer the light into the microscope and illuminate the sample through the glass substrate. The resulting light spot on the cross-section exhibited an area of about 1 mm^2. Tunable intensity supra-band-gap (405 nm, 3.06 eV, blue) and sub-band-gap (561 nm, 2.21 eV, green) lasers were used as the light source. To be able to measure the EBIC signal lock-in amplification was necessary over most of the illumination intensity range. Secondary electron and EBIC images were acquired simultaneously and could be compared and overlaid so that the physical origin of the EBIC signal could be

highlighted and beam exposure minimized. EBIC images were interpreted by simulating the EBIC profiles obtained, allowing identification of the space-charge region (SCR) and quasi-neutral region, as well as measurement of the collection length in the quasi-neutral region. The collection length in a *p*-*n* junction is determined by the diffusion length of minority carriers. Further details can be found in the Experimental Methods section and in the SI (S.1).

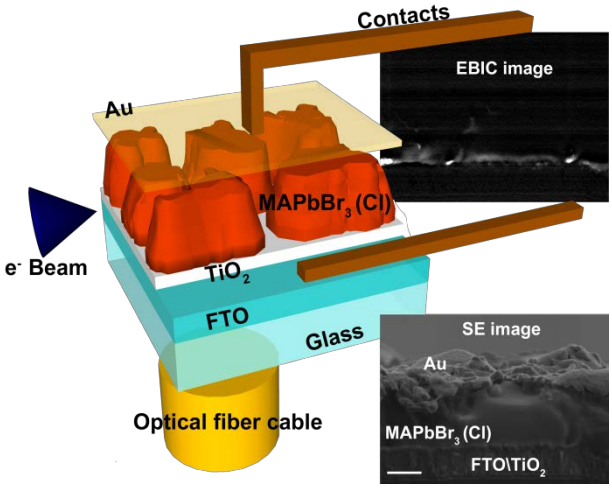

Figure 1: Layer stack of the $MAPbBr_3(Cl)$ solar cell, as well as the orientation of the electron beam and illumination during the EBIC measurement. The HTL, between $MAPbBr_3(Cl)$ and Au, is omitted in the picture for clarity. Corresponding secondary electron and EBIC images are also shown.

In figure 2, a *j*-*V* curve of our best performing solar cell is presented. Its photovoltaic parameters, along with the averages for all devices, are given in table 1. Forward and reverse scans are highlighted, indicating a hysteresis, which mostly affects the V_{oc} and the fill factor (*FF*). Our device areas are 0.16 cm^2, and a typical solar-cell device exhibited a V_{oc} of 1.35-1.45 V with a j_{sc} value of up to 5 mA/cm^2 and a *FF* of 0.65, adding up to an average efficiency of 4% under AM1.5 standard illumination conditions. Even though the HTL and TiO_2 are in direct contact, the interface is rectifying with a forward bias breakdown voltage higher than the cell's V_{OC} so it does not shunt the device. Hysteresis is present in this type of device mainly as differences in V_{OC} and FF between forward and reverse scans. A 0.05 – 0.07V difference in V_{OC} is commonly observed between forward and reverse scans for a scan rate of 0.05 V/sec. Discussion of why hysteresis does not impact the results below is presented in the SI (S.2).

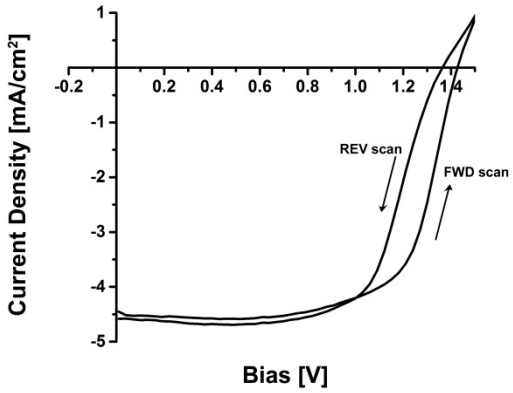

Figure 2 : Current-voltage plot in forward and reverse scan of the best solar cell used in the present work.

Table 1: Solar-cell parameters for forward and reverse scans of the best cell, as well as the average values for all solar cells analyzed.

	V_{oc} (V)	j_{sc} (mA/cm^2)	*FF* (%)	Eff (%)
FWD scan	1.42	4.5	70	4.4
REV scan	1.36	4.6	68	4.2
AVERAGE of all cells	1.35	4.1	65	3.4

The EBIC profile shape can be used to illustrate the spatial variation of the collection efficiency in the device. High collection efficiency can generally be attributed to the presence of a built-in field. In the quasi-neutral region, where collection is diffusion-limited, an exponential decay of the signal is expected (unless the L_n, L_p >> *d*, the active layer thickness). Further discussion and illustrations of the EBIC profiles expected from a *p*-*n* and *p*-*i*-*n* junction can be found in the SI (S.1 and Figure S1).

The EBIC profile of an $MAPbBr_3(Cl)$ solar cell in figure 3 exhibits characteristics of a *p*-*n* junction. A secondary electron image is shown next to the EBIC image, from which the current profile is extracted. The shape of the EBIC profile fits that of a *p*-*n* junction with a *n*-type FTO/TiO_2 and *p*-type $MAPbBr_3(Cl)$. The narrow plateau indicates the position of the space-charge region (SCR), with maximum collection probability. Since the space-charge region extends mainly within the *p*-type $MAPbBr_3(Cl)$, we can assume that the n-type doping in the TiO_2 is larger than the p-type doping in the perovskite. The EBIC signal decays towards the contacts, corresponding to the diffusion lengths of minority carriers. Depending on the sample, the space-charge-region width is in the range of 50-150 nm, and the average diffusion length for minority carriers in the dark L_n, ranges from 50 to 150 nm. To a large extent the variation in the minority carrier diffusion length arises from sample to sample differences. Within one sample, from grain to grain, the diffusion length standard deviation from the average is 25 nm.

The *p*-type nature of the Br perovskite has been suggested in the past both in experimental and theoretical papers[36,37]. Our EBIC results support this finding and illustrate for the first time the working mechanism of this photovoltaic device.

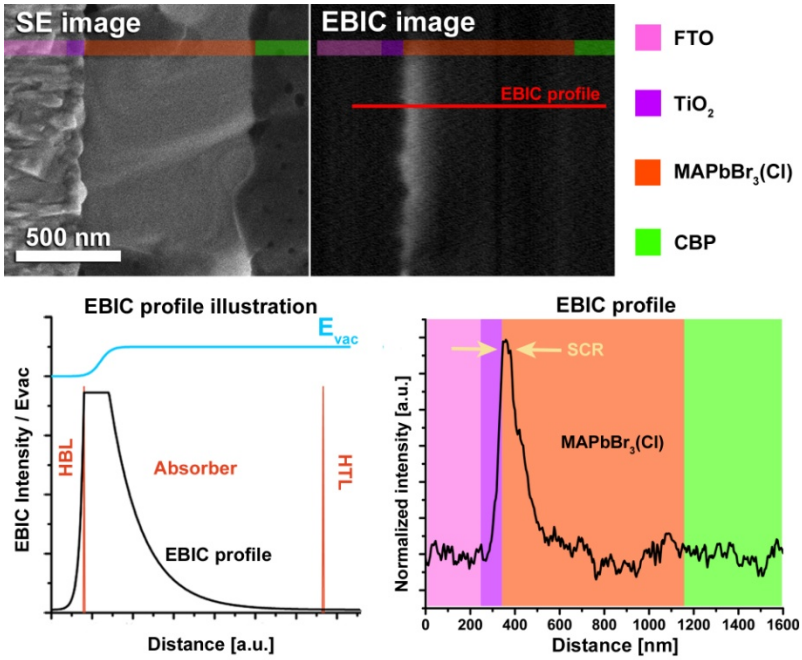

Figure 3: Secondary electron (top left) and the corresponding EBIC image (top right). The EBIC signal profile was extracted from the noted line in the EBIC image and is presented on the bottom right; it indicates a SCR width of 50 nm and electron diffusion length in the $MAPbBr_3(Cl)$ of 75 nm. At bottom left is an ideal picture illustrating how the EBIC profile and built-in field are related for comparison to the data.

Upon illumination using the supra-bandgap (blue, 405 nm) laser, the diffusion lengths calculated from the EBIC signal increased substantially (figure 4). At the highest attainable illumination, a diffusion length of up to L_n = 450 nm is measured, with an average of 360 ± 22 nm. The diffusion length is not uniform and can vary strongly within a single grain of the perovskite ranging from maximum to the dark value. The images in figure 4 illustrate the effect of light on carrier collection efficiency and diffusion length. Light intensity in this case was such that the sample current was about 20 nA. For this sample, under such illumination the electron diffusion length increases from L_n = 50 nm in the dark to about 110 nm (as illustrated in the EBIC profiles of figure 4), which increases the collection efficiency from the perovskite crystal substantially.

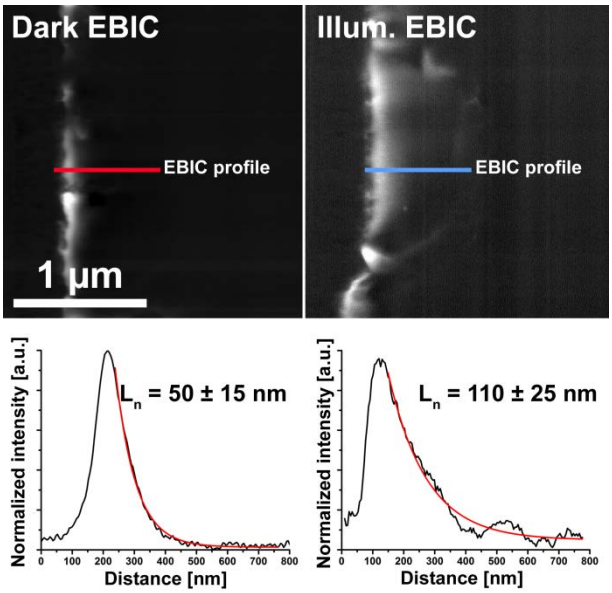

Figure 4: Comparison of EBIC images in the dark and under illumination generating ~20 nA photocurrent. The shown line profiles (taken from the lines shown in the images) were selected as they show signal decay corresponding to the average electron diffusion lengths for this sample. An alternative version of this figure, showing the location of the FTO/TiO_2 and HTL contacts is given in the SI section S.2.

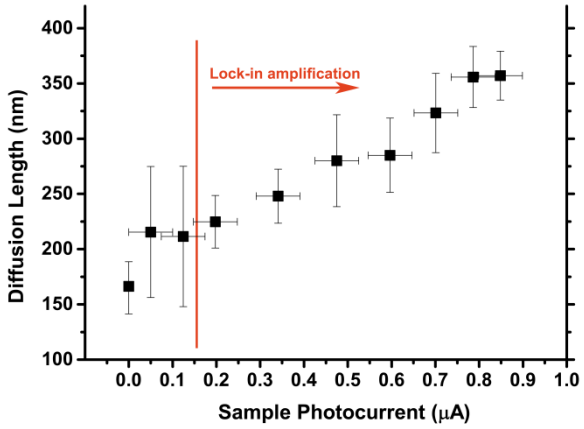

Figure 5: Electron diffusion length as a function of sample photocurrent. The photocurrent in this case is indicative of the light intensity. Vertical error bars are a standard deviation from the averaged diffusion length of various grains and show the variability of the diffusion length within the device. Under illumination higher noise than in the dark increases the uncertainty. Horizontal error bars represent the uncertainty in the measurement of the sample photocurrent.

In figure 5 the increase in average diffusion length vs. the measured sample photocurrent is shown. The photocurrent was measured immediately after the EBIC measurements while the beam was blanked. Inhomogeneity of the material spreads the calculated diffusion length over a large range. For this reason, the average value of the diffusion length was taken as representing the overall ability of electrons to diffuse in the material. The diffusion length was found to increase monotonically with light intensity, with maximum average value of L_n= 360 ± 22 nm at photon flux yielding 900 nA. Under our working conditions, the highest detected electron diffu-

sion length (450 nm) was 30% larger than the average, which suggests better uniformity will result in significant improvement of device performance. The diffusion length increase is expected to saturate (and possibly even decrease) at higher light intensities than those that could be used in the present work, owing to increased recombination rates under stronger illumination intensities, which may limit the carrier lifetime. The maximum diffusion length that we observed, even at the low light intensities available in our setup, are more than adequate to explain the J_{SC} measured in our devices. The analysis needed to reach this conclusion is presented in the SI (S.3).

The physical origin of the illumination effect is not simply the photogenerated increase in carrier density, because the excess free carrier concentration generated by the illumination is ~10^{14} cm^{-3}, i.e., far less than the estimated doping level of about 10^{17} cm^{-3} (see below). The carrier density generated by the e-beam is estimated to be about 10^{16}, at most 10^{17} cm^{-3}, *i.e.*, much higher than that due to illumination and approaching the doping level. To calculate the carrier density generated by the e-beam we have assumed a carrier lifetime of 50-100 ns[2,38] throughout the entire perovskite layer. A complete explanation of how this estimation was made can be found in the SI (S.4).

As the product of the diffusion coefficient and the carrier lifetime determines the diffusion length, $L_n = \sqrt{D\tau_n}$, the detected increase in diffusion length can be attributed to increases in the diffusion coefficient and/or in the lifetime of the carrier.

One possible explanation for larger minority carrier diffusion lengths under illumination is occupation of trap states, which would affect the lifetime of the charge carriers. However, trap filling is unlikely to be the cause in this case, because the e-beam induced carrier concentration is much higher than that generated by illumination, i.e., the illumination is unlikely to cause much change in trap state occupation. Thus, our analysis shows that the effect of illumination is not related to carrier concentration or trap filling.

To check whether supra-band-gap illumination is necessary, sub-band-gap illumination was applied by a green laser at 2.2 eV, just below the $MAPbBr_3(Cl)$ absorption edge of 2.3 eV. Under green laser illumination, we did not detect any change in the diffusion length, even at intensities (for the green laser power) equivalent to 1 sun, including the intensities used with the blue laser. From this finding we conclude that the increased diffusion length depends on photogeneration of carriers and not on the absolute carrier density. For $MAPbI_3$ thin films, structural and consequently electronic changes in the material, e.g., formation of domains which favor electron or hole conduction, were proposed to cause increased lifetime under illumination.[23,25–27] Stamplecoskie et al. suggested that for $MAPbI_3$, structural changes could occur through excitation of a charge transfer transition instead of a band-to-band transition, which they propose to explain transient absorption measurements.[39] Possibly a similar mechanism is at work for the $MAPbBr_3(Cl)$ thin films. If such a transition were present, it would require relatively narrow excitation energy and perhaps would not be excited by high-energy electron beam irradiation but only by light of appropriate wavelength. Clearly more work is needed to support this speculation to explain light-induced carrier lifetime improvement for the Br and the I perovskites or to test other hypotheses.

As an additional experiment, we investigated the changes in the EBIC signal under applied voltage. In view of the small changes in space charge region width observed at low bias, we restricted

the measurement to applied voltages of -1, 0, and +1 V. Higher bias voltages were avoided in order to prevent damage due to high currents. Figure 6 shows the resulting squared space-charge region width w^2 as a function of the applied voltage V_a. This plot also contains a linear fit, which allows a rough estimate of the general trend in space charge region width. Future work will explore this trend in more detail. We also performed this experiment under illumination generating 600 nA photocurrent, and found that values for the space-charge region width at the various applied voltages agreed with their dark values. Only larger diffusion length values were obtained under illumination and bias (figure S3), in good agreement to the result given in figure 5.

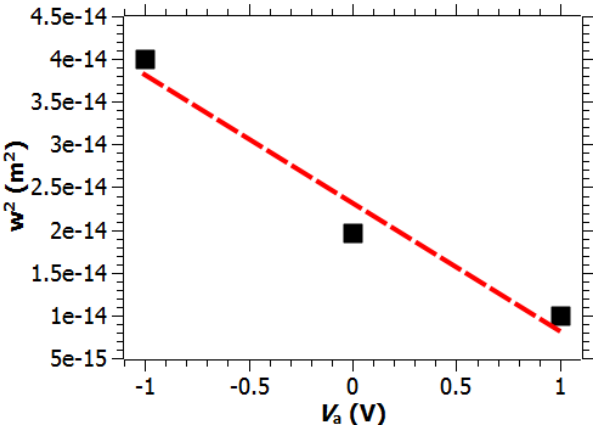

Figure 6: The squared space-charge region width w^2 as a function of the applied voltage V_a (black squares). The red dashed line represents a linear fit.

In order to gain further insight in the electrical properties of the FTO/TiO_2/$MAPbBr_3$(Cl)/CBP/Au solar cell stack, capacitance-voltage measurements were performed. The dielectric constant experienced by carriers in the space charge region (SCR) was estimated from the SCR width measured by EBIC and the SCR capacitance as determined by the impedance response of the PV device. The dielectric constant is estimated from the capacitance relationship $C/A=\varepsilon_0\varepsilon_r/w$ (where ε_0 is the vacuum permittivity, ε_r is the relative dielectric constant of $MAPbBr_3$(Cl), w is the space charge region width of about 150 nm, and A is the area of the capacitor). This analysis gives a relative dielectric susceptibility of $\varepsilon_r \approx 5 - 12$ at frequencies between 2 kHz to 1 MHz, which can be considered to be in reasonable agreement with the literature given the complexities of dielectric susceptibility in this material (see SI S.5). Use of this model requires careful consideration because of the complexities of the impedance spectrum and the non-uniform perovskite layer, which complicates the capacitor area, A. The net doping N_A in the $MAPbBr_3$(Cl) layer as a function of V_a was determined from the Mott-Schottky plot according to the relation $N_A = -2(e\varepsilon_s\, d(1/C^2)/dV)^{-1}$ (see figure 7)[40]. The values for the net doping are all in the order of 8×10^{17}- 7×10^{18} cm^{-3}, for values of V_a between -0.3 and +0.8 V. Outside of this bias interval, the capacitance measurements exhibited non-linear features, which did not allow for further evaluation. A complete description of the analysis is given in the SI (S.5).

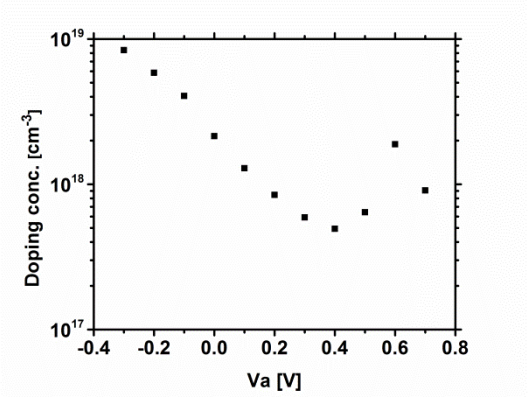

Figure 7: Doping concentration vs. applied voltage V_a (black squares), as derived from the derivative of the Mott-Schottky plot (SI Figure S5.)

Using the value of $\varepsilon_r \approx 5 - 12$, also the EBIC data shown in figure 6 allow for an estimate of the net doping in the $MAPbBr_3(Cl)$ layer. For simplicity, we assume a n^+-p junction and an entirely depleted space-charge region, i.e., the width of the space-charge region can be approximated by $w^2=2\varepsilon_0\varepsilon_r(V_{bi}-V_a)/eN_A$[41], where V_{bi} and e are the built-in potential and the elemental charge. We obtain estimates of $V_{bi} = 1.5 \pm 0.2$ V and a carrier concentration of $N_A = 3\text{-}6\times10^{17}$ cm^{-3}, which is in agreement with the carrier concentration obtained by capacitance-voltage measurement.

The *p-n* working mechanism observed in this study may be a result of the relatively high doping of our $MAPbBr_3(Cl)$ material. Doping of hybrid organic-inorganic lead trihalide perovskites is not yet well understood, poorly controlled, and may differ from deposition to deposition as well as vary between research groups. While the vast work invested in the iodide perovskite allows some controlled synthesis of lower-doped material, this is not yet the case for the bromide analog. As the diffusion length of minority carriers is inherently dependent on the majority carrier concentration,[41] a lower doped layer is expected to yield higher performance when used in solar cells, with longer "dark" drift/diffusion length. Lower doping will also result in a wider SCR, which will improve charge separation and collection. The doping may even be reduced to the extent that the cell will perform as a p-i-n junction similarly to the iodide case. Because unfortunately no material properties except optical bandgaps tend to be included in reports on Br-perovskite devices, we cannot exclude at this point the possibility that for devices, reported in the literature, the doping density of the perovskite material differs from what we report here.

In summary, EBIC shows evidence for the *p-n* nature of our $FTO/TiO_2/MAPbBr_3(Cl)/CBP/Au$ solar cells. Furthermore, EBIC measurements of the minority carrier diffusion length in $MAPbBr_3(Cl)$ show it to be affected by supra-bandgap illumination of the sample. Starting from "dark" values of 100 ± 50 nm, the diffusion length increases to 360 ± 22 nm under 3-4 % full sun equivalent illumination. From EBIC at applied voltage, and from capacitance-voltage measurements, we estimate the net doping of our $MAPbBr_3(Cl)$ thin films to be $N_A = 3\text{-}6 \times 10^{17}$ cm^3.

Our finding emphasizes and adds to increasing experimental evidence that the hybrid organic-inorganic lead halide perovskite materials differ, at least in some aspects, from "classical" semiconductors and dark measurements may not be representative of the relevant properties.

Experimental Methods

The solar cells were prepared by spray-coating a planar TiO_2 layer on FTO, onto which the 3:1 MABr : $PbCl_2$ perovskite solution in DMF was spin-coated to form $MAPbBr_3(Cl)$ (see endnote 19 concerning the notation (Cl)). The HTL used for high voltage cells (V_{oc} > 1V) is 4,4'-bis(N-carbazolyl)-1 ,1' –bisphenyl (CBP) doped with Li(trifluoromethane)$_2$-sulfonimide (LiTFSI), spin-coated from chlorobenzene. Because of the crystallization kinetics of $MAPbBr_3(Cl)$, the perovskite layer is non-continuous with many places where CBP is in direct contact with the TiO_2. Finally, Au is evaporated through a shadow mask as back contact to complete the cell. The full procedure is described in the SI (S.6).

Sample transfer to the scanning electron microscope was kept short, in order to reduce contamination of the cross-section surface. We used a Zeiss scanning electron microscope fitted with a pre-amplifier to amplify the EBIC current, a beam blanker to modulate the electron beam, and a lock-in amplifier to isolate the beam-generated signal. This setup allows for acquiring electron and EBIC images simultaneously. For the perovskites in particular, care must be taken to avoid beam damage, which can affect the measured properties. The generated carrier concentration, which depends on beam current and beam energy, should be kept low in order to avoid reaching a high injection regime, which might not be representative of the cell function under one sun illumination. The SEM beam blanker was operated within a frequency range of 500 Hz - 15 kHz. Within this range, the solar cell capacitance was found not to affect the results. Due to beam damage considerations the lock-in amplifier time constant was adjusted to a few ms, which resulted in the low frequency (< 1kHz) modulated EBIC being affected by high noise and therefore only frequencies of 5 kHz or higher were used. The full EBIC setup details including beam damage information can be found in the SI (S.7-S.9).

The illumination intensity was adjusted by setting the laser power and by using a cross polarizer. Up to a light intensity which gives ~ 100 nA of photocurrent (over the ~ 1 mm^2 spot), DC measurements could be performed. At intensities corresponding to photocurrent in the range of 200 – 900 nA, lock-in amplification had to be used. The highest light intensity corresponds to a photon flux equivalent to a few percent of 1 sun. At higher light intensity the EBIC signal to background level was too low even for lock-in amplification. In the case of the sub-bandgap green 2.21 eV irradiation, no readjustment of the "dark" measurement parameters was required as no detectable photocurrent was produced.

In order to compare EBIC profiles under dark and light conditions, two approaches were used. In the first approach the same location was imaged twice, under illumination and in the dark. Special attention to the effect of beam damage is needed using this approach. Imaging was therefore limited to fast scan rates and low pixel exposure times. In addition the order of dark-light measurements was changed to get an idea of the effect of beam damage. The second, less restrictive approach is to image a pristine part of the sample every time. To be able to get a statistically significant result in this way at least 5 images were taken at a particular light intensity and 25 EBIC profiles were extracted from each image.

EBIC images were interpreted by simulating the EBIC profiles obtained, using the charge collection model of Donolato[42] to distinguish between the space charge region (SCR) and quasi-neutral

region, and to measure their extent and the decay rate of the signal in the latter. For low-injection conditions, Donolato described the EBIC signal acquired at a *p-n* junction as a convolution of a lateral generation profile and a collection function ranging from the edge of the space-charge region (SCR) to the back contact. With the boundary conditions of complete collection in the SCR and translation invariance parallel to the p-n junction, the model is reduced into one dimension (perpendicular to the p-n junction). During interpretation of EBIC profiles, care must be taken to identify artifacts that can arise. This is discussed in SI (S.2) specifically for the case of distinguishing artifacts from true signal generation in the (thin) contact materials.

Acknowledgements

All WIS authors thank the Leona M. and Harry B. Helmsley Charitable Trust, the Israel National Nano-Initiative, the Israel Ministry of Science, and the Nancy and Stephen Grand Center for Sensors and Security for partial support. All HZB authors acknowledge the financial support of the Helmholtz Virtual Institute Microstructure Control in Thin-Film Solar Cells, VI-520. We thank S. Kirmayer, T. Kirchartz, R. Klenk, and M.D. Heinemann for helpful discussion of the results and H. Stapel and H. Joachimi (Point Electronic GmbH) for technical support. T.M.B. thanks the WIS for an Alternative Sustainable Energy Initiative (AERI) postdoctoral fellowship. D.C. holds the Sylvia and Rowland Schaefer Chair in Energy Research.

Supporting Information Available: SI includes more detailed presentation of EBIC data analysis, estimation of dielectric constant and doping density and experimental procedures. This material is available free of charge via the Internet: http://pubs.acs.org.

References

(1) Heo, J. H.; Song, D. H.; Im, S. H. Planar $CH_3NH_3PbBr_3$ Hybrid Solar Cells with 10.4% Power Conversion Efficiency, Fabricated by Controlled Crystallization in the Spin-Coating Process. *Adv. Mater.* **2014**, *26*, 8179–8183.

(2) Sheng, R.; Ho-Baillie, A.; Huang, S.; Chen, S.; Wen, X.; Hao, X.; Green, M. A. Methylammonium Lead Bromide Perovskite-Based Solar Cells by Vapor-Assisted Deposition. *J. Phys. Chem. C* **2015**, *119*, 3545–3549.

(3) Ryu, S.; Noh, J. H.; Jeon, N. J.; Kim, Y. C.; Yang, W. S.; Seo, J.; Seok, S. I. Voltage Output of Efficient Perovskite Solar Cells with High Open-Circuit Voltage and Fill Factor. *Energy Environ. Sci.* **2014**, *7*, 2614–2618.

(4) Edri, E.; Kirmayer, S.; Kulbak, M.; Hodes, G.; Cahen, D. Chloride Inclusion and Hole Transport Material Doping to Improve Methyl Ammonium Lead Bromide Perovskite-Based High Open-Circuit Voltage Solar Cells. *J. Phys. Chem. Lett.* **2014**, *5*, 429–433.

(5) Rühle, S.; Segal, A.; Vilan, A.; Kurtz, S. R.; Grinis, L.; Zaban, A.; Lubomirsky, I.; Cahen, D. A Two Junction, Four Terminal Photovoltaic Device for Enhanced Light to Electric Power Conversion Using a Low-Cost Dichroic Mirror. *J. Renew. Sustain. Energy* **2009**, *1*, 013106.

(6) Kim, S.; Kasashima, S.; Sichanugrist, P.; Kobayashi, T.; Nakada, T.; Konagai, M. Development of Thin-Film Solar Cells Using Solar Spectrum Splitting Technique. *Sol. Energy Mater. Sol. Cells* **2013**, *119*, 214–218.

(7) Bard, A. J.; Fox, M. A. Artificial Photosynthesis: Solar Splitting of Water to Hydrogen and Oxygen. *Acc. Chem. Res.* **1995**, *28*, 141–145.

(8) Jacobsson, T. J.; Fjällström, V.; Sahlberg, M.; Edoff, M.; Edvinsson, T. A Monolithic Device for Solar Water Splitting Based on Series Interconnected Thin Film Absorbers Reaching over 10% Solar-to-Hydrogen Efficiency. *Energy Environ. Sci.* **2013**, *6*, 3676–3683.
(9) Tachibana, Y.; Vayssieres, L.; Durrant, J. R. Artificial Photosynthesis for Solar Water-Splitting. *Nat. Photonics* **2012**, *6*, 511–518.
(10) Edri, E.; Kirmayer, S.; Mukhopadhyay, S.; Gartsman, K.; Hodes, G.; Cahen, D. Elucidating the Charge Carrier Separation and Working Mechanism of CH3NH3PbI3−xClx Perovskite Solar Cells. *Nat. Commun.* **2014**, *5*, 3461.
(11) Edri, E.; Kirmayer, S.; Henning, A.; Mukhopadhyay, S.; Gartsman, K.; Rosenwaks, Y.; Hodes, G.; Cahen, D. Why Lead Methylammonium Tri-Iodide Perovskite-Based Solar Cells Require a Mesoporous Electron Transporting Scaffold (but Not Necessarily a Hole Conductor). *Nano Lett.* **2014**, *14*, 1000–1004.
(12) Kim, H.-S.; Mora-Sero, I.; Gonzalez-Pedro, V.; Fabregat-Santiago, F.; Juarez-Perez, E. J.; Park, N.-G.; Bisquert, J. Mechanism of Carrier Accumulation in Perovskite Thin-Absorber Solar Cells. *Nat. Commun.* **2013**, *4*, 2242.
(13) Gonzalez-Pedro, V.; Juarez-Perez, E. J.; Arsyad, W.-S.; Barea, E. M.; Fabregat-Santiago, F.; Mora-Sero, I.; Bisquert, J. General Working Principles of $CH_3NH_3PbX_3$ Perovskite Solar Cells. *Nano Lett.* **2014**, *14*, 888–893.
(14) Marchioro, A.; Teuscher, J.; Friedrich, D.; Kunst, M.; van de Krol, R.; Moehl, T.; Grätzel, M.; Moser, J.-E. Unravelling the Mechanism of Photoinduced Charge Transfer Processes in Lead Iodide Perovskite Solar Cells. *Nat. Photonics* **2014**, *8*, 250–255.
(15) Leamy, H. J. Charge Collection Scanning Electron Microscopy. *J. Appl. Phys.* **1982**, *53*, R51–R80.
(16) Tanaka, K.; Takahashi, T.; Ban, T.; Kondo, T.; Uchida, K.; Miura, N. Comparative Study on the Excitons in Lead-Halide-Based Perovskite-Type Crystals $CH_3NH_3PbBr_3$ $CH_3NH_3PbI_3$. *Solid State Commun.* **2003**, *127*, 619–623.
(17) Saba, M.; Cadelano, M.; Marongiu, D.; Chen, F.; Sarritzu, V.; Sestu, N.; Figus, C.; Aresti, M.; Piras, R.; Lehmann, A. G.; et al. Correlated Electron–hole Plasma in Organometal Perovskites. *Nat. Commun.* **2014**, *5*, 5049.
(18) D'Innocenzo, V.; Grancini, G.; Alcocer, M. J. P.; Kandada, A. R. S.; Stranks, S. D.; Lee, M. M.; Lanzani, G.; Snaith, H. J.; Petrozza, A. Excitons versus Free Charges in Organo-Lead Tri-Halide Perovskites. *Nat. Commun.* **2014**, *5*, 3586.
(19) There has been some controversy around the presence and amount of chloride in perovskite formed from Cl containing precursors, and we do not wish to address this here. We simply denote $MAPbI_3$ prepared with one chloride-containing precursor as $MAPbI_3$(Cl) and will do likewise for the analogous bromide. In this work we deal only with $MAPbBr_3$(Cl).
(20) Stranks, S. D.; Eperon, G. E.; Grancini, G.; Menelaou, C.; Alcocer, M. J. P.; Leijtens, T.; Herz, L. M.; Petrozza, A.; Snaith, H. J. Electron-Hole Diffusion Lengths Exceeding 1 Micrometer in an Organometal Trihalide Perovskite Absorber. *Science* **2013**, *342*, 341–344.
(21) Xing, G.; Mathews, N.; Sun, S.; Lim, S. S.; Lam, Y. M.; Grätzel, M.; Mhaisalkar, S.; Sum, T. C. Long-Range Balanced Electron- and Hole-Transport Lengths in Organic-Inorganic $CH_3NH_3PbI_3$. *Science* **2013**, *342*, 344–347.
(22) Dong, Q.; Fang, Y.; Shao, Y.; Mulligan, P.; Qiu, J.; Cao, L.; Huang, J. Electron-Hole Diffusion Lengths > 175 mm in Solution-Grown $CH_3NH_3PbI_3$ Single Crystals. *Science* **2015**, *347*, 967–970.
(23) Gottesman, R.; Haltzi, E.; Gouda, L.; Tirosh, S.; Bouhadana, Y.; Zaban, A.; Mosconi, E.; De Angelis, F. Extremely Slow Photoconductivity Response of $CH_3NH_3PbI_3$ Perovskites Suggesting Structural Changes under Working Conditions. *J. Phys. Chem. Lett.* **2014**, *5*, 2662–2669.

(24) Juarez-Perez, E. J.; Sanchez, R. S.; Badia, L.; Garcia-Belmonte, G.; Kang, Y. S.; Mora-Sero, I.; Bisquert, J. Photoinduced Giant Dielectric Constant in Lead Halide Perovskite Solar Cells. *J. Phys. Chem. Lett.* **2014**, *5*, 2390–2394.
(25) Brivio, F.; Walker, A. B.; Walsh, A. Structural and Electronic Properties of Hybrid Perovskites for High-Efficiency Thin-Film Photovoltaics from First-Principles. *APL Mater.* **2013**, *1*, 042111.
(26) Even, J.; Pedesseau, L.; Katan, C. Analysis of Multivalley and Multibandgap Absorption and Enhancement of Free Carriers Related to Exciton Screening in Hybrid Perovskites. *J. Phys. Chem. C* **2014**, *118*, 11566–11572.
(27) Frost, J. M.; Butler, K. T.; Brivio, F.; Hendon, C. H.; van Schilfgaarde, M.; Walsh, A. Atomistic Origins of High-Performance in Hybrid Halide Perovskite Solar Cells. *Nano Lett.* **2014**, *14*, 2584–2590.
(28) Stoumpos, C. C.; Malliakas, C. D.; Kanatzidis, M. G. Semiconducting Tin and Lead Iodide Perovskites with Organic Cations: Phase Transitions, High Mobilities, and Near-Infrared Photoluminescent Properties. *Inorg. Chem.* **2013**, *52*, 9019–9038.
(29) Xiao, Z.; Yuan, Y.; Shao, Y.; Wang, Q.; Dong, Q.; Bi, C.; Sharma, P.; Gruverman, A.; Huang, J. Giant Switchable Photovoltaic Effect in Organometal Trihalide Perovskite Devices. *Nat. Mater.* **2015**, *14*, 193–198.
(30) Meier, S. B.; Tordera, D.; Pertegás, A.; Roldán-Carmona, C.; Ortí, E.; Bolink, H. J. Light-Emitting Electrochemical Cells: Recent Progress and Future Prospects. *Mater. Today* **2014**, *17*, 217–223.
(31) Riess, I. Voltage-Controlled Structure of Certain P-N and P-I-N Junctions. *Phys. Rev. B* **1987**, *35*, 5740–5743.
(32) Marsh, R. A.; McNeill, C. R.; Abrusci, A.; Campbell, A. R.; Friend, R. H. A Unified Description of Current–Voltage Characteristics in Organic and Hybrid Photovoltaics under Low Light Intensity. *Nano Lett.* **2008**, *8*, 1393–1398.
(33) Koster, L. J. A.; Mihailetchi, V. D.; Xie, H.; Blom, P. W. M. Origin of the Light Intensity Dependence of the Short-Circuit Current of Polymer/fullerene Solar Cells. *Appl. Phys. Lett.* **2005**, *87*, 203502.
(34) Donolato, C. Evaluation of Diffusion Lengths and Surface Recombination Velocities from Electron Beam Induced Current Scans. *Appl. Phys. Lett.* **1983**, *43*, 120–122.
(35) Luke, K. L.; Roos, O. von; Cheng, L. Quantification of the Effects of Generation Volume, Surface Recombination Velocity, and Diffusion Length on the Electron- beam- induced Current and Its Derivative: Determination of Diffusion Lengths in the Low Micron and Submicron Ranges. *J. Appl. Phys.* **1985**, *57*, 1978–1984.
(36) Dymshits, A.; Rotem, A.; Etgar, L. High Voltage in Hole Conductor Free Organo Metal Halide Perovskite Solar Cells. *J. Mater. Chem. A* **2014**, *2*, 20776–20781.
(37) Shi, T.; Yin, W.-J.; Hong, F.; Zhu, K.; Yan, Y. Unipolar Self-Doping Behavior in Perovskite $CH_3NH_3PbBr_3$. *Appl. Phys. Lett.* **2015**, *106*, 103902.
(38) Zhang, M.; Yu, H.; Lyu, M.; Wang, Q.; Yun, J.-H.; Wang, L. Composition-Dependent Photoluminescence Intensity and Prolonged Recombination Lifetime of Perovskite $CH_3NH_3PbBr_{3-x}Cl_x$ Films. *Chem. Commun.* **2014**, *50*, 11727–11730.
(39) Stamplecoskie, K. G.; Manser, J. S.; Kamat, P. V. Dual Nature of the Excited State in Organic–inorganic Lead Halide Perovskites. *Energy Environ. Sci.* **2014**, *8*, 208–215.
(40) Singh, J. *Semiconductor Devices: Basic Principles*, First Edition.; Wiley, 2000.
(41) Sze, Min, S. *Physics of Semiconductor Devices*, Third Edition.; Wiley, 2007.
(42) Donolato, C. An Alternative Proof of the Generalized Reciprocity Theorem for Charge Collection. *J. Appl. Phys.* **1989**, *66*, 4524–4525.